energy&fuels

pubs.acs.org/EF

Article

Nickel MXene Nanosheet and Heteroatom Self-Doped Porous Carbon-Based Asymmetric Supercapacitors with Ultrahigh Energy Density

Om Priya Nanda, Aksha Gilbert Prince, Lignesh Durai, and Sushmee Badhulika*

Cite This: *Energy Fuels* 2023, 37, 4701−4710

Read Online

ACCESS | Metrics & More | Article Recommendations | Supporting Information

ABSTRACT: For high-energy-density supercapacitors, two-dimensional (2D) MXenes are being increasingly explored due to their inherent conductivity and excellent chemical properties. However, MXenes failed to achieve high power density and exceptional stability. Addressing this, we report the fabrication of an asymmetric supercapacitor with nickel MXene (cathode) and nitrogen (N), sulfur (S), and phosphorus (P) self-doped biomass-derived activated carbon (anode). Detailed structural and chemical characterization studies reveal layered nanosheets in NiMX caused due to solvothermal etching cum exfoliation and unique micro−mesopore distribution in the optimized *Euphorbia milii* plant leaf-derived heteroatom self-doped activated carbon (EMAC-700) because of KOH activation. NiMX and EMAC-700 delivered high capacitances of 474.3 and 575.8 F/g, respectively, at 1 A/g with a 6 M KOH electrolyte. This is attributed to the pseudonature of NiMX and the presence of heteroatoms and the large surface area (2349 m^2/g) of EMAC-700, facilitating fast electrolytic ion transfer. Finally, an asymmetric device with NiMX//EMAC configuration in 6 M KOH delivered a 152.6 F/g cell capacitance at 0.5 A/g under 0−1.5 V. Additionally, an ultrahigh energy density of 47.6 W h/kg at a 375 W/kg power density was achieved along with an 81.7% capacitance retention after 30,000 cycles at 15 A/g, signifying its potential for next-generation energy storage applications.

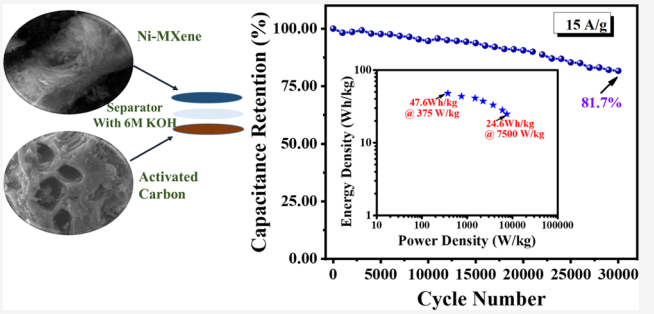

1. INTRODUCTION

Supercapacitors have drawn significant interest in the energy storage field because of their fast charging and discharging rates, high power density, and exceptional cycle stability.[1] Thus, they show potential in a number of applications where long cycle life with high power is widely desired, ranging from cars and portable electronics to military equipment.[2] Such properties of supercapacitors are decided via the charge storage mechanisms as well as the associated kinetics at the electrode/electrolyte interface. Supercapacitors generally store energy either by an electrostatic adsorption−desorption process referred to as electric double-layer capacitors (EDLCs), where electrolyte ions diffuse without any charge transfer into the pores of carbon materials. Hence, the amount of surface area that the electrolyte ions can access limits their capacity, thus providing high power density but suffering from low specific capacitance, resulting in low energy density.[3] However, it can also store energy through a reversible redox reaction process by using mobile metal ions (pseudocapacitor), which deliver excellent energy density but lag in terms of power density. So, to overcome the shortcomings of both mechanisms, a new approach of combining both by using a pseudocapacitive material as a cathode and an EDLC material as an anode is being explored to achieve superior performance.[4]

Recently, 2D transition-metal nitrides and carbides, named MXenes, have drawn significant interest for pseudocapacitors owing to their exceptional metallic electrical conductivity as well as their highly reversible surface redox properties.[5] MXenes commonly have a 2D hexagonal structure having an $M_{n+1}X_nT_x$ configuration and $P6_3/mmc$ symmetry; here, M belongs to transition metals such as V, Fe, Ti, and so forth, and X stands for nitride or carbide, whereas T represents surface functional groups like _O, _F, and _OH that cause hydrophilic nature of MXenes.[6]

Typically, ternary layered ceramic materials called MAX phases are used in the synthesis of MXenes. The MAX phases are denoted by the formula $M_{n+1}AX_n$, where M stands for metals like V, Ti, Cr, Mo, Ta, and Nb, A belongs to elements of groups 13 or 14 like Si and Al, and X is nitrogen (N) and/or

Received: January 6, 2023
Revised: February 26, 2023
Published: March 7, 2023

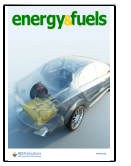

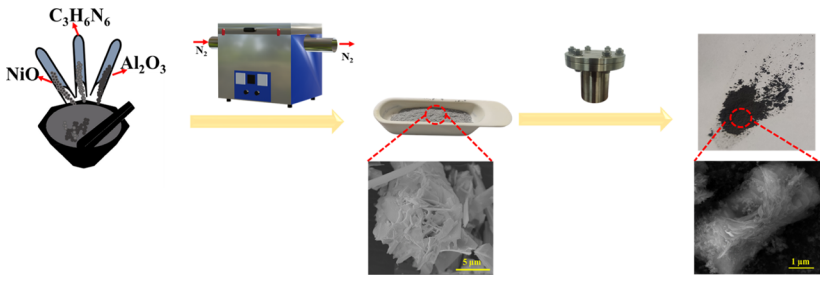

Figure 1. Graphical representation of the synthesis of NiMX nanosheets via a combination of annealing and solvothermal etching processes.

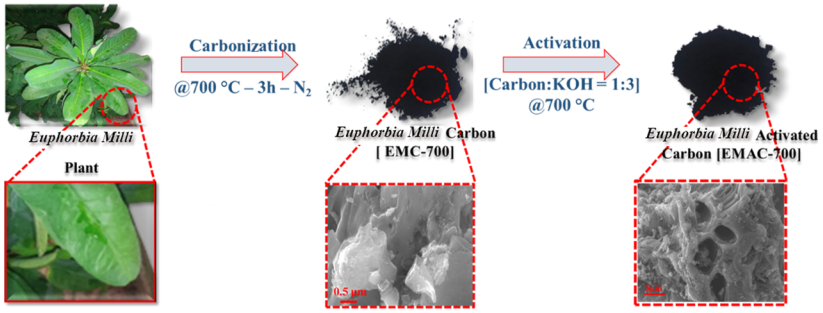

Figure 2. Schematic view of solid-state synthesis of EMAC-700 from Euphorbia plant leaves via the KOH activation process.

carbon (C), having n = 1, 2, or 3.[5] Mostly, for electrochemical processes, nickel-based MXene (NiMX) can be an ideal option because of its ability to achieve multiple stable oxidation states (Ni^{2+} and Ni^{3+}); nickel (Ni) is an eminent electrocatalyst with admirable redox activity that promises excellent pseudocapacitive behavior, while C increases the material's conductivity and gives the system mechanical stability.

Generally, activated carbon, CNTs, and graphene possess high surface area and are employed for EDLC applications.[7] In particular, biowaste-derived activated carbon has received widespread attention because of its fast regeneration, easy availability, and low production cost with a significant contribution to solid waste management.[8] Though activated carbons have a high surface area that undergoes fast adsorption−desorption of charges and results in high power density, they do not yield good energy density. In this context, to enhance the capacitive effect, heteroatom doping has been introduced, which induces more defects and improves surface wettability, thereby resulting in improved energy density.[9,10] For EDLC application, numerous biowaste sources such as food waste, corn husk, bamboo waste, sugarcane bagasse, and so forth are already being used as a source for preparing activated carbon.[8]

In this work, NiMX nanosheets have been employed as a cathode along with the optimized EMAC as an anode for designing an asymmetric supercapacitor device in order to attain high power and energy density. Here, NiMX is synthesized via solid-state reaction synthesis of the MAX compound Ni_3AlC_2 (NiMAX), followed by etching and exfoliation of layers to form Ni_3C MXene (NiMX) nanosheets via the solvothermal method. Along with this, *Euphorbia milii* plant leaf waste-derived activated porous carbon is optimized based upon three different temperatures, namely, 650, 700, and 800 °C wherein EMAC obtained at 700 °C showed superior results. So, EMAC-700 was taken further for subsequent measurements. To the best of our knowledge, this is the first report on nickel-based MXene with *E. milii*-derived activated carbon for asymmetric supercapacitor applications.

2. EXPERIMENTAL SECTION

2.1. Materials and Reagents. For the carbon source, *E. milii* plant leaves were collected from the IIT Hyderabad campus. Aluminum oxide (Al_2O_3; 99.9%), nickel oxide (NiO; 98%), potassium hydroxide (KOH; 85%), ammonium fluoride (NH_4F; 99%), hydrochloric acid (HCl; 38%), melamine powder ($C_3H_6N_6$; 99%), polyvinylidene difluoride (PVDF, Mw ∼ 53,4000), acetylene black, *N*-methyl-2-pyrrolidone (NMP, 99.5%), and ethanol were bought from Sigma-Aldrich, and deionized (DI) water was taken from a Millipore system.

2.2. Material Characterization and Instrumentation. The morphological studies of NiMX and EMAC-700 were examined using a Zeiss Ultra-55 scanning electron microscope and JEOL 2100 transmission electron microscope. To obtain the pore size distribution and surface area, Brunauer−Emmett−Teller (BET) analysis was done (model: Quantachrome ASiQwin). The crystallographic structure and phase were observed using X-ray diffraction [XRD, Model: Lineon X'Pert PRO X-ray diffractometer (source: Cu Kα (λ = 1.54 Å)] at a 2θ ranging from 5 to 80°. The surface functional groups present in the material were examined using Fourier transform infrared (FT-IR, model: IR Affinity spectrophotometer, spectral range: 500−3500 cm^{-1}) spectroscopy. The chemical bonding and state of the molecular system were studied via Raman scattering [model: Witec Alpha 300 confocal Raman microscope, source: λ = 532 nm (spectral range: 100−1800 cm^{-1})]. The compositional studies were done via X-ray photoelectron spectroscopy (XPS, model Scienta Omicron ESCA$^+$).

2.3. Synthesis of NiMX from NiMAX. This NiMX was synthesized via a high-temperature synthesis technique which is a recently reported work from our lab.[6] In brief, stoichiometric quantities of NiO, Al_2O_3, and $C_3H_6N_6$ were mixed thoroughly to attain fine powder by using a mortar and pestle. The mixture was annealed at 900 °C in a N_2 atmosphere for 3 h, and after cooling down to ambient temperature, it was ground to a fine powder to obtain Ni_3AlC_2 nanoflakes (NiMAX) as shown in eq 1.[6]

The exfoliation and etching of NiMAX were performed to achieve a few layered Ni_3C (NiMX) nanosheets. In brief, an equimolar solution of HCl and NH_4F was prepared in the presence of 10% (w/v) of NiMAX by ultrasonication for 0.5 h. The attained NiMAX-containing solution was solvothermally treated at 200 °C for 5 h, and the as-attained product was repeatedly washed using DI water and ethanol till pH (=7) and dehydrated at 70 °C to produce NiMX. Figure 1

https://doi.org/10.1021/acs.energyfuels.3c00085
Energy Fuels 2023, 37, 4701−4710

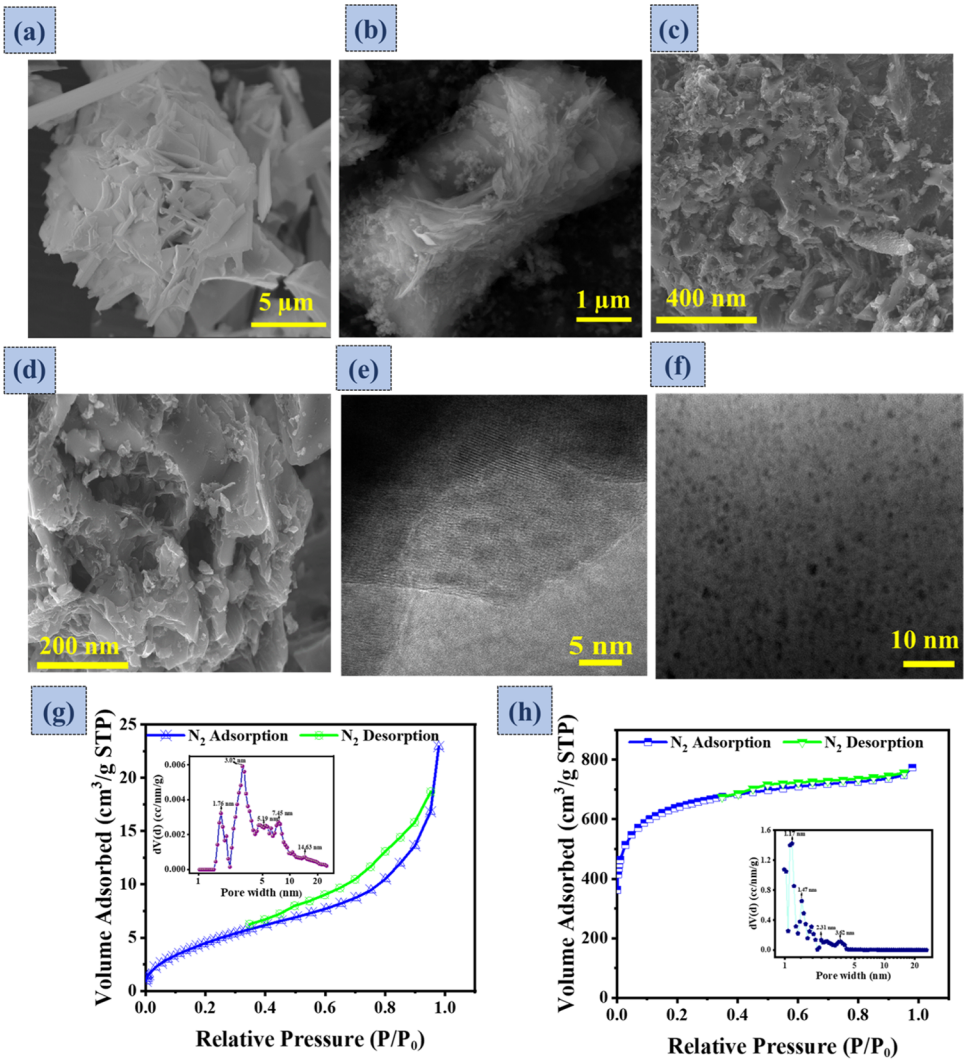

Figure 3. SEM micrographs of (a) NiMAX, (b) NiMX, and (c) EMAC-700 at lower magnification, (d) EMAC-700 at higher magnification, TEM micrographs of (e) NiMX and (f) EMAC-700, and N_2 adsorption−desorption isotherms of (g) NiMX (inset: pore size distribution) and (h) EMAC-700 (inset: pore size distribution).

presents the synthesis method of NiMAX followed by the exfoliation and etching process to achieve a few layered NiMX nanosheets.

$$12NiO + 2Al_2O_3 + 4C_3H_6N_6 \rightarrow 4Ni_3AlC_2 + 4CO_2 + 10NO + 12H_2 + 7N_2 \quad (1)$$

2.4. Synthesis of N, S, and P Self-Doped Activated Carbon. *E. milii* leaves collected from the IIT Hyderabad campus were repeatedly cleaned with water and then air-dried at 80 °C for 10 h. The dried leaves were crushed into a fine powder and pyrolyzed at two distinct temperatures (i.e., 700 and 800 °C) for 3 h in a N_2 atmosphere using a tubular furnace and were named as EMC-700 and EMC-800, respectively. The carbonized sample was washed with 3 M HCl for the removal of inorganic impurities and other byproducts. The carbon was then activated using KOH (ratio—EMC/KOH = 1:3) at two distinct temperatures (i.e., 700 and 800 °C) and named as EMAC-700 and EMAC-800, respectively. A graphical view of the synthesis procedure is exhibited in Figure 2. Due to the superior outcome of EMAC-700 as compared to EMAC-800, the optimized EMAC-700 was used for subsequent studies. This material has also been recently reported from our lab.[10]

2.5. Fabrication of Electrodes. EMACs and NiMX were taken separately as the active material, and then carbon black and PVDF were added as conductive additives and binders, with a ratio of 75:15:10, respectively. Then, using a pestle and mortar, the mixture was ground with a simultaneous dropwise addition of NMP to prepare a slurry. In addition to this, nickel foam (NF) current collectors were cut into 3 cm × 1 cm and a circular shape with a 1 cm diameter to be used in half-cell and full-cell studies, respectively. After cutting, NFs were cleaned with DI water, acetone, and IPA via ultrasonication for 15 min each and then dried at 80 °C for 1 h. Then, the obtained slurry was coated on the NF over 1 cm × 1 cm for half-cell studies, and circular NFs were coated fully (1 cm diameter) for full-cell fabrication. The coated NFs were then dried at 120 °C for 10 h to obtain electrodes.

2.6. Electrochemical Measurements. The MXene and EMAC-700 modified electrodes were tested with a 6 M KOH electrolyte in a 3E setup at 0 to 0.5 V and −1 to 0 V potential windows, respectively. Here, the modified electrode was employed as a working electrode, while platinum wire (Pt) and Hg/HgO were used as the counter and reference electrodes, respectively. In addition to this, to check the practicability, an asymmetric cell (coin cell-CR2032) was also fabricated. Cyclic voltammetry (CV), galvanostatic charge−discharge (GCD), and electrochemical impedance spectroscopy (EIS) in the frequency range of 0.1−100 kHz were done using CHI 660E. Supporting Information Section I contains the charge balance of the device along with the detailed formulae used to calculate the specific capacitance (F/g), energy density (W h/kg), and power density (W/kg).

https://doi.org/10.1021/acs.energyfuels.3c00085
Energy Fuels 2023, 37, 4701−4710

3. RESULTS AND DISCUSSION

Among both the EMACs, EMAC-700 has superior electrochemical performance as compared to EMAC-800 in the three-electrode configuration, data given in S4 in the Supporting Information. Hence, EMAC-700 was used for subsequent studies. The optimized EMAC-700 and NiMX were analyzed thoroughly by physiochemical characterizations as well as electrochemical measurements, and their characteristic properties are discussed in detail.

3.1. Physiochemical Characterization. *3.1.1. Morphological Analysis.* The surface morphology of both NiMX and EMAC-700 was analyzed via SEM micrographs. Figure 3a depicts the SEM image of the NiMAX phase, signifying the existence of nanoflake stacking, while Figure 3b illustrates the SEM image of NiMX showing the formation of clustered folded sheet-like structures. This demonstrates the presence of nanosheets in NiMX, which is due to the enhanced interlayer bonding caused by newly etched layers via solvothermal etching. The as-formed 2D structures shorten the diffusion path, which is advantageous for ion and electron transport, thereby enhancing the pseudocapacitance.[5] In the case of EMAC-700, a large number of pores were observed. Figure 3d,e shows the morphology of EMAC-700 at lower and higher magnifications, demonstrating a thick layer-like structure with an obvious distribution of pores on it due to the chemical activation using KOH at high temperatures. As KOH melts and penetrates into the carbon sample at higher temperatures, it leaves behind vacant pores upon being cleaned with HCl. As a result, a large surface area of porous carbon formed, which is highly desirable for supercapacitor applications. Figure 3e, depicting the TEM image of NiMX, confirms the folded nanosheet-like structure. The existence of micropores in EMAC-700 with unique distribution is also confirmed by the TEM micrograph, as shown in Figure 3f. Additionally, SEM and TEM micrographs of the NiMAX phase are given in Figure S1 of the Supporting Information. The EDS analysis is also given in Figures S2 and S3 for NiMX and EMAC-700, respectively.

The porosity and surface area of both NiMX and EMAC-700 were obtained via BET analysis. Figure 3g depicts the type-II adsorption−desorption isotherm of NiMX with an 18 m^2/g surface area, and the average pore size of NiMX was found to be 3.03 nm with a 0.027 cm^3/g pore volume. Figure 3h, showing an assortment of type-I and IV isotherms for EMAC-700 with a steep increase in adsorption at $P/P_0 < 0.01$ (very low relative pressure), demonstrates the existence of supermicropores (<2 nm) as well as the presence of mesopores (H4-hysteresis). This also resulted in a 2349.6 m^2/g surface area, which holds a promise of higher electrolytic diffusion of ions, thereby enhancing the EDLC behavior.[11] Furthermore, the pore-size distribution curve provides additional evidence of EMAC-700 having a large microporous framework with few over the surface. The highest value noticed was 3.62 nm, after which no increment was observed. In addition to this, the pore volume of EMAC-700 was observed to be 1.055 cm^3/g. In Table 1, a piece of detailed information about the surface area, pore width, and pore volume of both samples is shown.

3.1.2. Structural Analysis. The detailed structural analysis of the as-synthesized NiMAX has been provided in the Supporting Information. The crystalline-phase formation of NiMX and EMAC-700 has been determined via XRD spectra shown in Figure 4a. NiMX shows sharp peaks, which indicates its crystalline nature, while the absence of sharp peaks in EMAC-700 corresponds to its amorphous nature. In case of NiMX, the diffraction peaks observed at 2θ = ∼43, ∼44, ∼51, and ∼76° are attributed to (006), (113), (116), and (119) planes. This crystalline rhombohedral phase Ni_3C diffraction pattern matches well with JCPDS card no. 00-006-0697.[11] However, broadened peaks at 22.6 and 43.45° are ascribed to (002) and (100) crystal planes, respectively, noted in EMAC-700. Here, the (002) plane is attributed to the graphitic layers which are stacked parallelly in a coherent manner, which indicates the presence of aromatic carbons with random orientations, while the (100) plane demonstrates the existence of a higher-degree graphitic carbon structure.

Table 1. BET Results of NiMX and EMAC-700

sample	surface area (m^2/g)	average pore size (nm)	pore volume (cm^3/g)
NiMX	18.3	3.03	0.027
EMAC-700	2349.6	1.178	1.055

Furthermore, through FTIR analysis, NiMX and EMAC-700's surface functional groups were observed and are depicted in Figure 4b. The peaks witnessed at ∼ 3221, ∼1410, and ∼584 cm^{-1} are ascribed to −OH, N═O, and Ni−C−Ni, respectively,[12] which indicate the presence of metal by corroborating well with XRD. In addition to this, EMAC-700 showed characteristic peaks at ∼3440, ∼2887, ∼2341, ∼1640, ∼1250, and ∼1054 cm^{-1} attributed to −OH, C−H, CO_2 gas phase, C═C, C≡N, and C═O, respectively.[13,14] This specifies the self-doping of heteroatoms like nitrogen as well as oxygen in EMAC-700, which is effective for improving the wettability.

To obtain the chemical bonding of as-synthesized samples, Raman spectroscopy was done as depicted in Figure 4c. Both NiMX and EMAC-700 have similar characteristic peaks at ∼1345 cm^{-1} ascribed to the defect-induced D band, indicating the presence of disordered carbon, and the peak at ∼1600 cm^{-1} is attributed to the in-plane vibrational G band, demonstrating the existence of graphitic carbon.[15] The I_D/I_G ratio of NiMX and EMAC-700 was found to be 0.87 and 0.96, respectively. This comparatively low I_D/I_G value of NiMX corresponds to the large ordering of the sp^2 graphitic domains, hence holding the promise of a good graphitic structure. Furthermore, the higher I_D/I_G value (0.96) of EMAC-700 corresponding to a larger number of defects can be attributed to the presence of heteroatoms (N, S, and P) and KOH activation as well, which leads to enhancement of the wettability and rate of ion diffusion, thereby promising superior electrochemical behavior.

3.1.3. Chemical Analysis. To identify the elemental composition and binding energy states of both NiMX and EMAC-700, XPS was done and it is shown in Figure 5. From the complete survey spectrum of NiMX exhibited in Figure 5a, the peaks observed in NiMX confirm the existence of Ni and C atoms and other peaks in the survey spectrum, which indicates the presence of surface functional elements like O 1s and N 1s as it is adsorbed on the material surface to create stability. In addition to this, traces of elemental F are present as HF was used as an etchant and it is difficult to remove entirely even after cleaning multiple times. For a better understanding of individual elements in NiMX, high-resolution spectra of N 2p and C 1s are shown in Figure 5b,c. The XPS spectrum of Ni atoms indicates that 2p orbitals, $2p_{3/2}$, and $2p_{1/2}$ were ascribed

https://doi.org/10.1021/acs.energyfuels.3c00085
Energy Fuels 2023, 37, 4701−4710

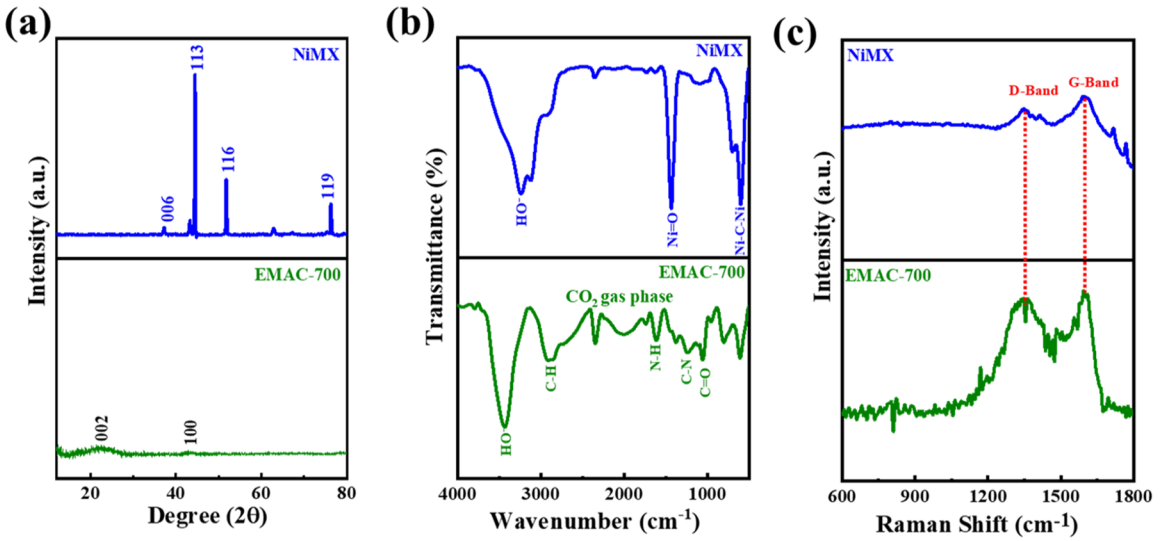

Figure 4. (a) XRD, (b) FTIR spectroscopy, and (c) Raman spectroscopy analysis of NiMX and EMAC-700.

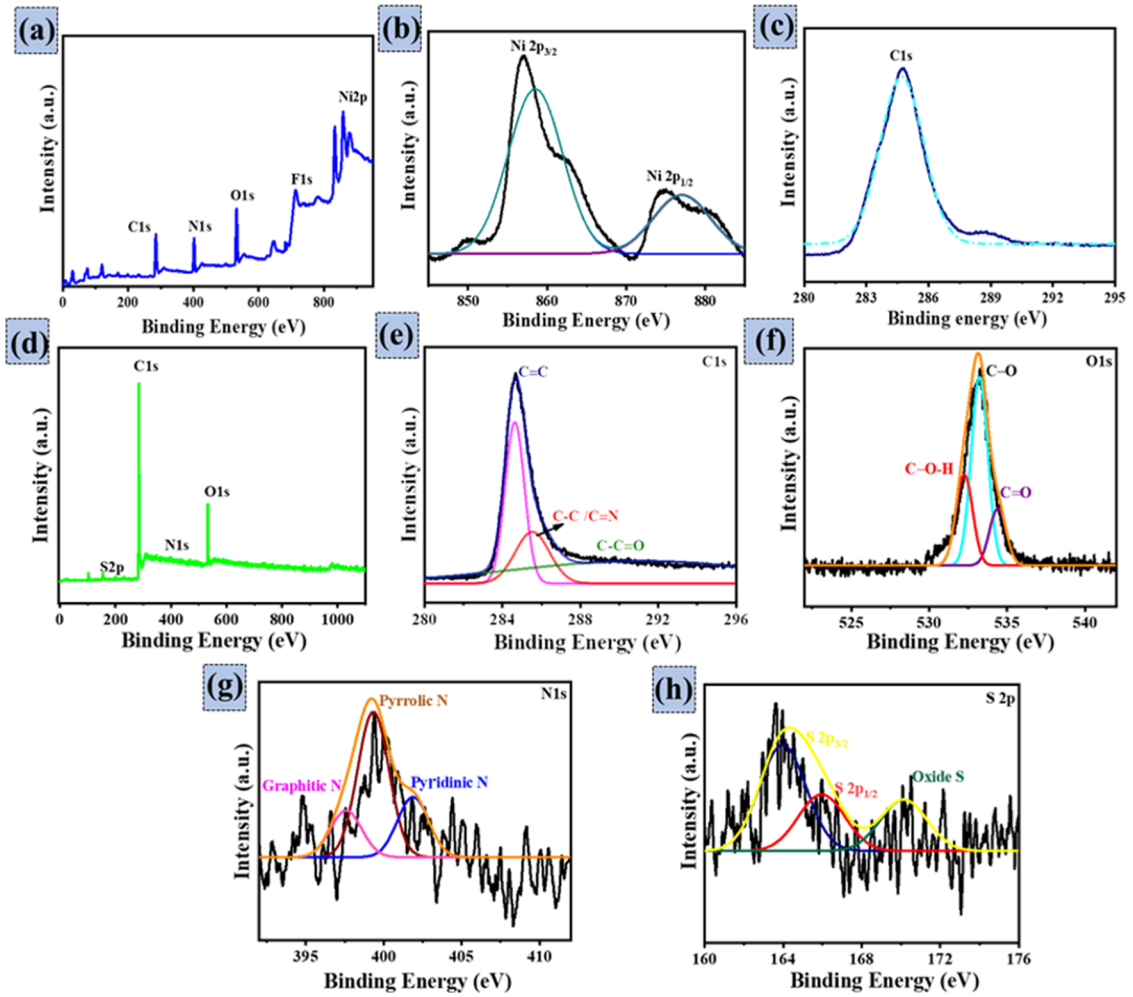

Figure 5. XPS (a) full survey spectra of NiMX, high-resolution spectra of (b) Ni 2p and (c) C 1s. (d) Full survey spectra of EMAC-700 and high-resolution spectra of (e) C 1s, (f) O 1s, (g) N 1s, and (h) S 2p.

to the NiMX bond formation, as shown in Figure 5b. At the same time, Figure 5c depicts the 1s molecular orbital of C. This suggests that Ni and C have a covalent bond, unless the material has been treated with external reducing or oxidizing agents. Hence, it further motivates to achieve high electrocatalytic activity of NiMX, favoring good electrochemical performance. In the case of EMAC-700, the complete survey spectrum given in Figure 5d confirms the existence of C, N, O,

https://doi.org/10.1021/acs.energyfuels.3c00085
Energy Fuels 2023, 37, 4701−4710

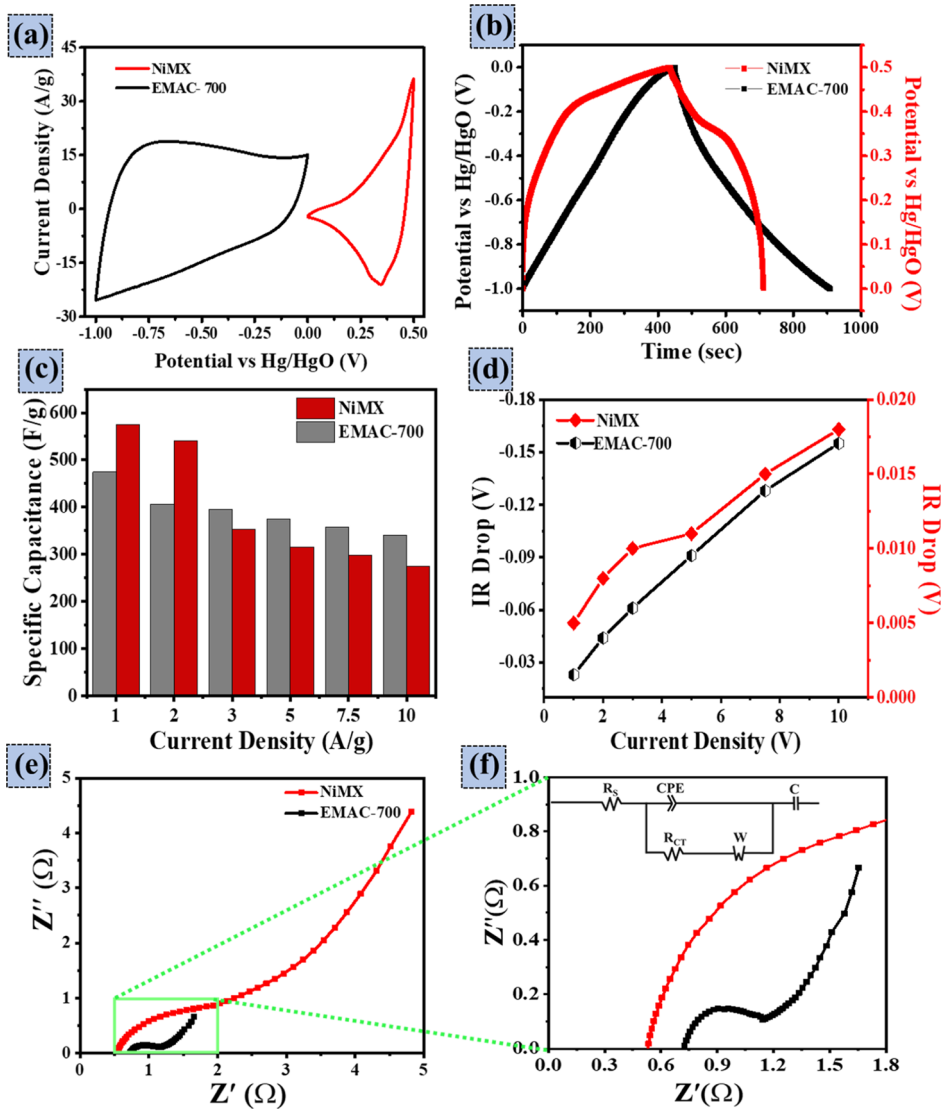

Figure 6. (a) CV curves at 50 mV/s, (b) GCD graphs at 1 A/g, (c) specific capacitance, (d) *IR* drop observed from 1 to 10 A/g current density, (e) EIS plot, and (f) magnified EIS (inset: equivalent circuit) of NiMX and EMAC-700 in 3E configurations with a 6 M KOH electrolyte.

and S heteroatoms, confirming the self-doping as no external source was used. The high-resolution C 1s spectra given in Figure 5e represent peaks at (I) 284 eV (C═C/C−C) showing the existence of graphitic carbon and (ii) 289.2 eV signifying the O−C═O bonds.

Additionally, the high-resolution O 1s spectra given in Figure 5f depict two peaks at 533.6 and 534.3 eV, attributed to C−O and C═O, correspondingly; this signifies more defects in carbon structures which would enhance the energy storage capability. Furthermore, the high-resolution N 1s spectra exhibit three peaks at 397.5, 399.4, and 401.83 eV, attributed to pyridinic N, pyrrolic N, and graphitic N, as depicted in Figure 5g. This graphitic N enhances the ion transport, while the pores are favored by the pyridinic and pyrrolic N.[16] Additionally, the high-resolution S 2p spectra depicted in Figure 5h showed three peaks of S $2p_{3/2}$, S $2p_{1/2}$, and oxidized sulfur attributed to 164.03, 165.9, and 170.06 eV, respectively, which will improve the surface wettability.

3.2. Electrochemical Measurements. Detailed electrochemical behaviors of NiMX and EMAC-700 were investigated by using CV, GCD, and EIS in a three-electrode (3E) configuration as well as an asymmetric full-cell device with a 6 M KOH supporting electrolyte.

3.2.1. In 3E Configuration. In a 3E configuration, the electrochemical behavior of NiMX and EMAC-700 was tested across positive (0−0.5) and negative potential windows (−1 to 0 V). CV at 50 mV/s depicted in Figure 6a demonstrates a redox curve of NiMX with a small peak at ∼0.35 V, indicating the pseudonature, whereas the quasi-rectangular shape of EMAC-700 signifies the EDLC nature with a minor pseudoeffect.[17] The presence of redox peaks in NiMX can be attributed to the adsorption and desorption of OH^- ions from the electrolyte on the electrode surface as well as the formation of functional groups and interaction of Ni ions with them, thereby undergoing oxidation and reduction.[18,19] At 1 A/g, GCD curves further confirm the nature of both NiMX and EMAC-700 as shown in Figure 6b. NiMX showed ideal faradic or battery-like behavior of charging−discharging with negligible *IR* drop corresponding to high specific capacitance (C_{SP}), while EMAC-700 further confirmed the synergistic effect of heteroatoms and wide distribution of micro−mesopores, inducing minor pseudobehavior to EDLC. With the rise in

https://doi.org/10.1021/acs.energyfuels.3c00085
Energy Fuels 2023, 37, 4701−4710

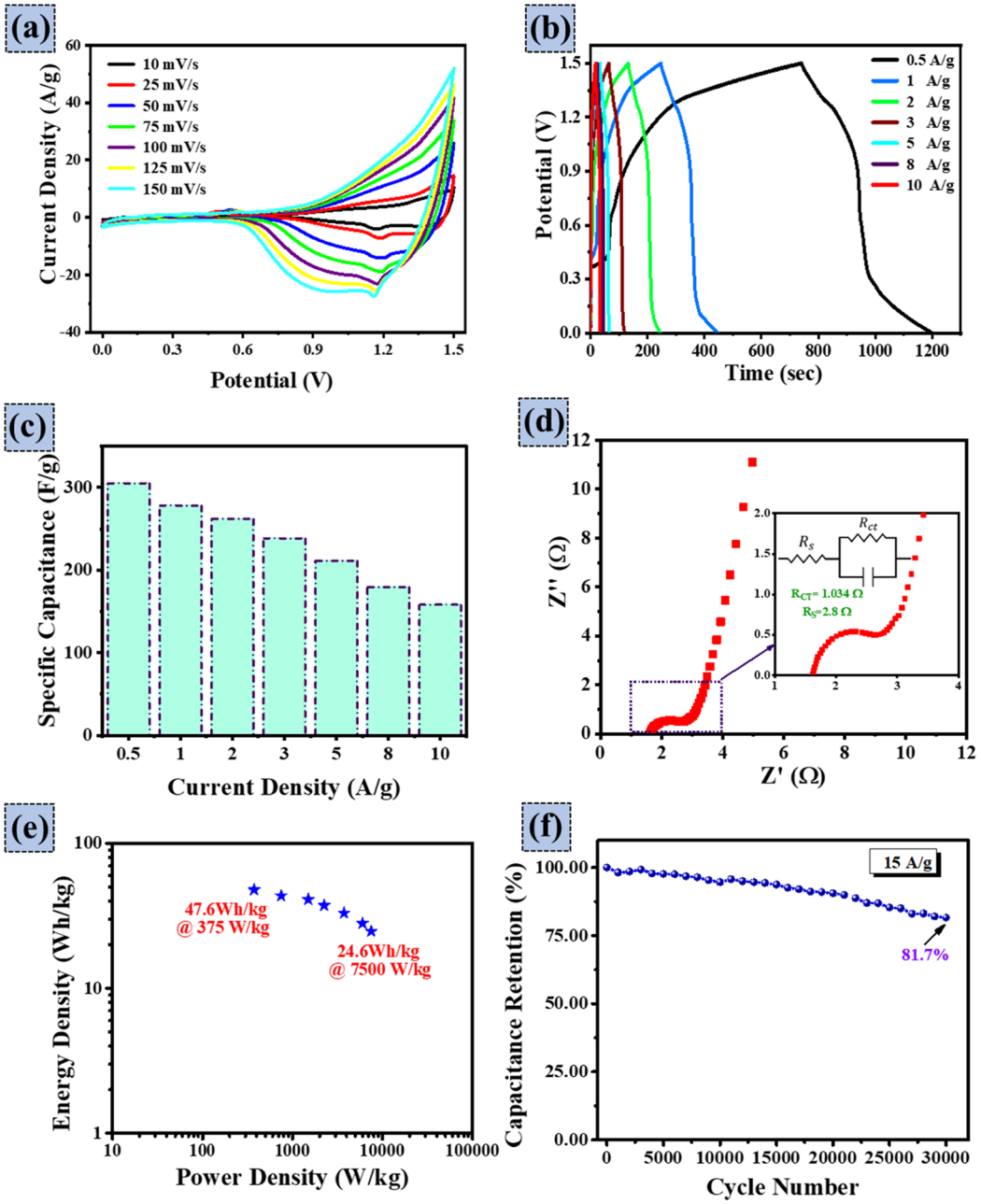

Figure 7. (a) Different scan rate CV curves, (b) different current density GCD graphs, (c) cell capacitance, and (d) EIS plot; inset—enlarged EIS with an equivalent circuit. (e) Ragone plot and (f) cyclic stability of the NiMX//EMAC-700 asymmetric device.

current density, C_{SP} decreased, whereas the *IR* drop (Ohmic resistance) increased due to reduced active ion interactions on the electrode surface.[20] In addition, NiMX showed a 575.8 F/g CSP with a small IR drop of 0.005 V at 1 A/g, which reduced to 274 F/g, whereas the IR drop value slightly increased to 0.018 V at 10 A/g, thus indicating low capacitance retention of NiMX. In the case of EMAC-700, the C_{SP} observed at the same 1 A/g was 474.3 F/g with a comparatively higher IR drop value of −0.023 V, which signifies that the Ohmic resistance of NiMX is lower than that of EMAC-700. Furthermore, the C_{SP} of EMAC-700 observed at 10 A/g was 340.69 F/g representing high rate capability (~82.3%). Detailed information about the C_{SP} and *IR* drop values obtained at different current densities for both compounds are compared and depicted in Figure 6c,d, respectively.

The EIS graph shown in Figure 6e demonstrates that NiMX has a high value of equivalent series resistance (ESR), that is, 2.23 Ω, while for EMAC-700, it is only 1.14 Ω (almost half). This is due to the easy ion diffusion in EMAC-700 owing to its micro−mesopores. In addition to this, the R_{CT}s obtained for NiMX and EMAC-700 were 1.68 and 0.45 Ω, respectively. This is because of the presence of heteroatoms and their porous nature, which results in acceleration of the ion transfer kinetics.[21] For a better understanding, an enlarged graph showing R_S and R_{CT} is shown in Figure 6f. The electrochemical performances of NiMX and EMAC-700 are detailed in Supporting Information Section II Figures S4 and S5, respectively.

3.2.2. In Asymmetric Cell Arrangement. The practicability of NiMX and EMAC-700 was evaluated by fabricating an

https://doi.org/10.1021/acs.energyfuels.3c00085
Energy Fuels 2023, 37, 4701−4710

Table 2. Comparison Table for Supercapacitive Performance of MXene-Based Asymmetric Supercapacitors

material	electrolyte	potential window (V)	specific capacitance	energy density (W h/kg)	power density (W/kg)	stability	refs
50MXene-50Ni(OH)$_2$//PC	3 M KOH + 0.1 M [$K_4Fe(CN)_6$] in PVA	1.6		29.3	800	90% after 5000 cycles	18
$CoNi_2S_4$//MAC	1 M KOH	1.6	155.75 F/g @ 2 A/g	55.37	3200	90.03% after 5000 cycles	25
Nb_2CT_X/CNT//AC	1 M H_2SO_4	1.5	51 F/g @ 2mV/s	16.5	375.2	73.3% after 2000 cycles	26
VN/AC//$Ti_3C_2T_X$	6 M KOH	1.68	70.2 F/g @ 0.5A/g	12.81	985.8	73% after 10,000 cycles	27
$Ti_3C_2T_X$//rGO/CNT/PANI	3 M H_2SO_4	1.45	116.9 F/g @ 10 mV/s	28.6	590	80% after 10,000 cycles	28
V_2CT_X//AC	2 M $ZnSO_4$	1.8	76 F/g @ 1 A/g	34	954	79% after 100,000 cycles @10 A/g	29
NiMX//EMAC-700	6 M **KOH**	**1.5**	**152.6 F/g @ 0.5 A/g**	**47.6**	**375**	**81.7% after** 30,000 **cycles at** 15 **A/g**	**this work**

asymmetric coin cell device wherein NiMX was employed as the cathode and EMAC-700 as the anode under a 0−1.5 V potential window with a 6 M KOH electrolyte. The CV curves shown in Figure 7a depict distorted pseudocurves with a distinct reduction peak at ∼1.18 V, indicating the dominance of the NiMX material over EMAC-700. This holds the promise of good electrochemical performance of the device from the high current values observed from the CV curves.[22,23] Furthermore, CV curves retained their shape with a rise in scan rate to 150 mV/s, demonstrating remarkable reversibility and superior rate capability of the asymmetric cell. In addition to this, the GCD profiles shown in Figure 7b also show a similar pseudonature of the device with negligible *IR* drop. The cell capacitance (C_{cell}) attained at 0.5 A/g was 152.6 F/g due to the dominating pseudonature of the device, which reduced to 79 F/g at 10 A/g.

To know the resistance offered by the device, EIS was done and is shown in Figure 7d. The device exhibited a low ESR of 2.65 Ω, which indicates that the ESR of single electrodes in a half-cell was less, while their combination in the device increased the resistance. This suggests that NiMX//EMAC-700 is an ideal combination for asymmetric full cells. In addition to this, the device also showed a low R_S value of 1.62 Ω which includes the resistance offered by the electrode, electrolytic solution, and electrode−electrolyte interface and it is calculated from the Z'-axis intercept.[24] The R_{CT} value observed was 1.034 Ω which is the resistance offered by electrode materials. To demonstrate the feasibility of the NiMX//EMAC-700 device for real-time application, the Ragone plot is exhibited in Figure 7e. In this, an excellent energy density of 47.6 W h/Kg at a power density of 375 W/kg was obtained, and the energy density was reduced to 24.6 W h/kg when the power density resulted in 7500 W/kg. The obtained values are far superior to recently reported MXene-based asymmetric supercapacitors. Furthermore, the device demonstrated a remarkable stability of 81.7% after 30,000 cycles at 15 A/g, as depicted in Figure 6f. Such a superior performance of the device is due to several factors, including (i) stable nature of the anode and cathode and (ii) N, S, and P heteroatom-containing EMAC-700 with high surface area as well as numerous micro−mesopores that can have long-term storage of electrolyte and promote the incessant formation of the double layer. The synergistic combination of NiMX//EMAC-700 for asymmetric devices is a perfect configuration as NiMX has excellent conductivity, while EMAC-700 has numerous micro−mesopores.

The electrochemical performance of NiMX- and EMAC-700-based asymmetric supercapacitors is higher in comparison to that of recently reported MXene-based asymmetric supercapacitors as shown in Table 2. In all these reports, the poor performance could be ascribed to the (i) instability of MXene (i.e., Ti-, V-, and Nb-based MXene), (ii) incompatibility in the selection of the cathode and anode, and (iii) electrocatalytic activity of electrode materials.[18,25−29] By resolving this, we have demonstrated a highly stable nickel-based MXene and activated carbon-based supercapacitor with a 47.6 W h/kg energy density with outstanding stability representing an ideal combination for an asymmetric supercapacitor.

4. CONCLUSIONS

To summarize, an ultrahigh-energy-density asymmetric device was fabricated with nickel-based MXene (NiMX) as a cathode and N, P, and S self-doped biomass-derived activated carbon (EMAC-700) as an anode. NiMX was synthesized via hydrothermal etching, while EMAC-700 was prepared via KOH activation. The assembled NiMX//EMAC-700 asymmetric supercapacitor device showed excellent performance with a C_{cell} of 152.6 F/g at 0.5 A/g and an ultrahigh energy density of 47.6 W h/kg at a power density of 375 W/kg. Along with this, the device also demonstrated an outstanding capacitance retention of 81.7% even after 30,000 cycles at a high current density of 15 A/g. This superior electrochemical performance of NiMX//EMAC-700 indicates that it could be an ideal choice for a low-cost, superior-performance supercapacitor to meet high-energy as well as power needs.

■ ASSOCIATED CONTENT

Supporting Information

The Supporting Information is available free of charge at https://pubs.acs.org/doi/10.1021/acs.energyfuels.3c00085.

Equations for calculating electrochemical performance (ECP), FESEM and TEM of the NiMAX phase, EDS of NiMX, EDS of EMAC-700, compared ECP of EMAC-800 with EMAC-700 in a 3E configuration, ECP of NiMX in a 3E configuration, ECP of EMAC-700 in a 3E configuration, B value analysis, and Raman spectroscopy analysis of the NiMX electrode after 30,000 charge−discharge cycles (PDF)

■ AUTHOR INFORMATION

Corresponding Author

Sushmee Badhulika − *Department of Electrical Engineering, Indian Institute of Technology Hyderabad, Hyderabad*

https://doi.org/10.1021/acs.energyfuels.3c00085
Energy Fuels 2023, 37, 4701−4710

502285, India; orcid.org/0000-0003-3237-3031; Phone: 040-23016467; Email: sbadh@iith.ac.in

Authors

Om Priya Nanda − *Department of Electrical Engineering, Indian Institute of Technology Hyderabad, Hyderabad 502285, India;* orcid.org/0000-0002-8749-7982

Aksha Gilbert Prince − *Department of Electrical Engineering, Indian Institute of Technology Hyderabad, Hyderabad 502285, India*

Lignesh Durai − *Department of Electrical Engineering, Indian Institute of Technology Hyderabad, Hyderabad 502285, India;* orcid.org/0000-0003-0478-2727

Complete contact information is available at: https://pubs.acs.org/10.1021/acs.energyfuels.3c00085

Author Contributions

O.P.N: conceptualization, methodology, data curation, writing original draft preparation, writing—reviewing and editing; A.G.P: methodology, data curation. L.D: methodology, data curation, reviewing, and editing. S.B: conceptualization, funding acquisition, investigation, project administration, resources, supervision, writing—review & editing.

Notes

The authors declare no competing financial interest.

■ ACKNOWLEDGMENTS

S.B. acknowledges financial assistance from Defence Research and Development Organization funding (DRDO) grant # DYSL-SM/CARS-04.

■ REFERENCES

(1) Mensah-Darkwa, K.; Zequine, C.; Kahol, P. K.; Gupta, R. K. Supercapacitor energy storage device using biowastes: A sustainable approach to green energy. *Sustainability* **2019**, *11*, 414.

(2) Gao, H.; Xiao, F.; Ching, C. B.; Duan, H. High-performance asymmetric supercapacitor based on graphene hydrogel and nano-structured MnO2. *ACS Appl. Mater. Interfaces* **2012**, *4*, 2801−2810.

(3) Wang, J.; Tang, J.; Ding, B.; Malgras, V.; Chang, Z.; Hao, X.; Wang, Y.; Dou, H.; Zhang, X.; Yamauchi, Y. Hierarchical porous carbons with layer-by-layer motif architectures from confined soft-template self-assembly in layered materials. *Nat. Commun.* **2017**, *8*, 15717.

(4) Gopalakrishnan, A.; Raju, T. D.; Badhulika, S. Green synthesis of nitrogen, sulfur-co-doped worm-like hierarchical porous carbon derived from ginger for outstanding supercapacitor performance. *Carbon* **2020**, *168*, 209−219.

(5) Jiang, Q.; Kurra, N.; Alhabeb, M.; Gogotsi, Y.; Alshareef, H. N. All pseudocapacitive MXene-RuO2 asymmetric supercapacitors. *Adv. Energy Mater.* **2018**, *8*, 1703043.

(6) Gilbert Prince, A. G.; Durai, L.; Badhulika, S. Ni3C MXene nanosheets as an efficient binder-less electrocatalyst for oxygen evolution reaction. *FlatChem* **2022**, *36*, 100439.

(7) Abbas, Q.; Raza, R.; Shabbir, I.; Olabi, A. G. Heteroatom doped high porosity carbon nanomaterials as electrodes for energy storage in electrochemical capacitors: A review. *J. Sci.: Adv. Mater. Devices* **2019**, *4*, 341−352.

(8) Nanda, O. P.; Das, N. K.; Sekar, P.; Ramadoss, A.; Saravanakumar, B. Bio-waste derived self-templated, nitrogen self-doped porous carbon for supercapacitors. *Bioresour. Technol. Rep.* **2022**, *19*, 101198.

(9) Qu, J.; Geng, C.; Lv, S.; Shao, G.; Ma, S.; Wu, M. Nitrogen, oxygen and phosphorus decorated porous carbons derived from shrimp shells for supercapacitors. *Electrochim. Acta* **2015**, *176*, 982−988.

(10) Nanda, O. P.; Badhulika, S. Biomass derived Nitrogen, Sulphur, and Phosphorus self-doped micro-meso porous carbon for high-energy symmetric supercapacitor−With a detailed study of the effect of different current collectors. *J. Energy Storage* **2022**, *56*, 106042.

(11) Munir, A.; Haq, T.; Saleem, M.; Qurashi, A.; Hussain, S. Z.; Sher, F.; Ul-Hamid, A.; Jilani, A.; Hussain, I. Controlled engineering of nickel carbide induced N-enriched carbon nanotubes for hydrogen and oxygen evolution reactions in wide pH range. *Electrochim. Acta* **2020**, *341*, 136032.

(12) Durai, L.; Badhulika, S. A facile, solid-state reaction assisted synthesis of a berry-like NaNbO3 perovskite structure for binder-free, highly selective sensing of dopamine in blood samples. *New J. Chem.* **2019**, *43*, 11994−12003.

(13) Siengchum, T.; Isenberg, M.; Chuang, S. S. Fast pyrolysis of coconut biomass - An FTIR study. *Fuel* **2013**, *105*, 559−565.

(14) Gunasekaran, S. S.; Gopalakrishnan, A.; Subashchandrabose, R.; Badhulika, S. Single step, direct pyrolysis assisted synthesis of nitrogen-doped porous carbon nanosheets derived from bamboo wood for high energy density asymmetric supercapacitor. *J. Energy Storage* **2021**, *42*, 103048.

(15) Suo, N.; Huang, H.; Wang, X.; Hou, X.; Shao, Z.; Zhang, G. Facile synthesis and electrocatalytic performance for oxygen reduction of boron-doped carbon catalysts on graphene sheets. *Fuel Cells* **2021**, *21*, 328−336.

(16) Gopalakrishnan, A.; Badhulika, S. Effect of self-doped heteroatoms on the performance of biomass-derived carbon for supercapacitor applications. *J. Power Sources* **2020**, *480*, 228830.

(17) Iro, Z. S.; Subramani, C.; Dash, S. S. A brief review on electrode materials for supercapacitor. *Int. J. Electrochem. Sci.* **2016**, *11*, 10628−10643.

(18) Karmur, R. S.; Gogoi, D.; Das, M. R.; Ghosh, N. N. High-Performance Flexible Supercapacitor Device Composed of a Hierarchical 2-D MXene-Ni (OH) 2 Nanocomposite and Biomass-Derived Porous Carbon Electrodes. *Energy Fuels* **2022**, *36*, 8488−8499.

(19) Chen, X.; Zhu, J.; Cai, J.; Zhang, Y.; Wang, X. Nanosheets assembled layered MXene/MoSe2 nanohybrid positive electrode materials for high-performance asymmetric supercapacitors. *J. Energy Storage* **2021**, *40*, 102721.

(20) Cao, W.; Yang, F. Supercapacitors from high fructose corn syrup-derived activated carbons. *Mater. Today Energy* **2018**, *9*, 406−415.

(21) Gunasekaran, S. S.; Badhulika, S. High-performance solid-state supercapacitor based on sustainable synthesis of meso-macro porous carbon derived from hemp fibres via CO2 activation. *J. Energy Storage* **2021**, *41*, 102997.

(22) Paul, A.; Ghosh, S.; Kolya, H.; Kang, C. W.; Chandra Murmu, N. C.; Kuila, T. Synthesis of nickel-tin oxide/nitrogen-doped reduced graphene oxide composite for asymmetric supercapacitor device. *Chem. Eng. J.* **2022**, *443*, 136453.

(23) Zhang, W.; Qi, J.; Cao, T.; Lei, Z.; Ma, Y.; Liu, H.; Zhu, L.; Feng, X.; Wei, W.; Zhang, H. A facile method synthesizing marshmallow ZnS grown on Ti3C2 MXene for high-performance asymmetric supercapacitors. *J. Energy Storage* **2022**, *50*, 104652.

(24) Seenath, J. S.; Biswal, B. P. Construction of MXene-Coupled Nitrogen-Doped Porous Carbon Hybrid from a Conjugated Microporous Polymer for High-Performance Supercapacitors. *Adv. Energy Sustainability Res.* **2021**, *2*, 2000052.

(25) Siddiqa, A.; Padaki, M. High-Energy-Density Asymmetric Supercapacitor Based on Layered-Double-Hydroxide-Derived CoNi2S4 and Eco-friendly Biomass-Derived Activated Carbon. *Energy Fuels* **2022**, *36*, 13286−13295.

(26) Xiao, J.; Wen, J.; Zhao, J.; Ma, X.; Gao, H.; Zhang, X. A safe etching route to synthesize highly crystalline Nb2CTx MXene for high performance asymmetric supercapacitor applications. *Electrochim. Acta* **2020**, *337*, 135803.

(27) Venkateshalu, S.; Grace, A. N. Ti3C2Tx MXene and Vanadium nitride/Porous carbon as electrodes for asymmetric supercapacitors. *Electrochim. Acta* **2020**, *341*, 136035.

(28) Li, K.; Wang, X.; Wang, X.; Liang, M.; Nicolosi, V.; Xu, Y.; Gogotsi, Y. All-pseudocapacitive asymmetric MXene-carbon-conducting polymer supercapacitors. *Nano Energy* **2020**, *75*, 104971.
(29) Chen, W.; Zhang, L.; Ren, H.; Miao, T.; Wang, Z.; Zhan, K.; Yang, J.; Zhao, B. V2CTx MXene as novel anode for aqueous asymmetric supercapacitor with superb durability in ZnSO4 electrolyte. *J. Colloid Interface Sci.* **2022**, *626*, 59−67.

https://doi.org/10.1021/acs.energyfuels.3c00085
Energy Fuels 2023, 37, 4701−4710